

*promoting access to White Rose research papers*



**Universities of Leeds, Sheffield and York**  
**<http://eprints.whiterose.ac.uk/>**

---

This is an author produced version of a paper published in **Physica D: Nonlinear Phenomena**.

White Rose Research Online URL for this paper:  
<http://eprints.whiterose.ac.uk/7924/>

---

**Published paper**

Houghton, S.M., Tobias, S.M., Knobloch, E. and Proctor, M.R.E. (2009)  
*Bistability in the Complex Ginzburg-Landau Equation with Drift*. Physica D: Nonlinear Phenomena, 238 (2). pp. 184-196.

<http://dx.doi.org/10.1016/j.physd.2008.09.011>

---

# Bistability in the Complex Ginzburg-Landau Equation with Drift

S. M. Houghton <sup>a,\*</sup>, S. M. Tobias <sup>a</sup>, E. Knobloch <sup>b</sup> and M. R. E. Proctor <sup>c</sup>

<sup>a</sup>*School of Mathematics, University of Leeds, LS2 9JT, UK*

<sup>b</sup>*Department of Physics, University of California, Berkeley, CA 94720, USA*

<sup>c</sup>*DAMTP, Centre for Mathematical Sciences, Wilberforce Road, Cambridge, CB3 0WA, UK*

---

## Abstract

Properties of the complex Ginzburg-Landau equation with drift are studied focusing on the Benjamin-Feir stable regime. On a finite interval with Neumann boundary conditions the equation exhibits bistability between a spatially uniform time-periodic state and a variety of nonuniform states with complex time dependence. The origin of this behavior is identified and contrasted with the bistable behavior present with periodic boundary conditions and no drift.

*Key words:* Complex Ginzburg-Landau Equation, Bistability, Spatiotemporal Chaos

*PACS:* 05.45, 47.20.K, 47.32, 47.54, 95.30.Q

---

## 1. Introduction

The complex Ginzburg-Landau (hereafter CGL) equation is a prototype equation describing the evolution of an oscillatory instability in spatially extended driven dissipative systems. The equation arises in two ways, (i) as the evolution equation for the (complex) amplitude  $A$  of a spatially uniform oscillation near onset of instability, and (ii) as the amplitude equation for traveling wavetrains with order one wavenumber  $k$  and frequency  $\omega(k)$ . In a frame traveling at the group velocity  $\omega'(k)$  of the waves the two equations are the same. The resulting equation includes the effects of diffusion and dispersion, as well as nonlinear saturation and nonlinear frequency adjustment, and as such has been extensively studied [1,6], generally in unbounded or periodic domains with large spatial period. The properties of this equation, suitably scaled, depend on two parameters only. In the supercritical case the parameter plane is divided into two regions by the stability boundary of the Stokes solution. This solution, a nonlinear but spatially uniform oscillation, is unstable to long wavelength disturbances above this (Benjamin-Feir) boundary but stable below it. However, computations in the Benjamin-Feir stable regime reveal that in periodic domains of sufficiently large

spatial period the stable Stokes solution may coexist with a spatiotemporally intermittent state called defect chaos that appears to persist indefinitely [4]. In this state defects are created (or annihilated) when the complex amplitude  $A$  vanishes and the phase of  $A$  becomes undefined. Between these events the system is in a state of spatio-temporal chaos and if no defects form this state is called phase turbulence.

In the present paper we are interested in examining the simultaneous effects of drift and boundaries on the bistable Benjamin-Feir stable regime. The presence of boundaries prevents the transformation to the comoving frame, and hence the advection term must be retained. The choice of boundary conditions determines the fate of the Stokes solution. Both Dirichlet and Robin boundary conditions eliminate the Stokes solution and hence the bistability present in the Benjamin-Feir (BF) stable regime in an unbounded domain. Despite this much rich behavior remains. In a previous paper [19] we showed that in extended systems of this type with a preferred direction of propagation the onset of instability is shifted substantially from the onset of convective instability in an unbounded system, and is now associated with the first appearance of a global mode of the system. This in turn corresponds to the onset of absolute instability in the unbounded system. Moreover, the frequency of the waves is selected by the upstream boundary condition, at least near onset, and this in turn determines the wavenumber of the downstream disturbance. One finds that near onset the instability is localized near

---

\* Corresponding author.

*Email addresses:* [smh@maths.leeds.ac.uk](mailto:smh@maths.leeds.ac.uk) (S. M. Houghton),

[smt@maths.leeds.ac.uk](mailto:smt@maths.leeds.ac.uk) (S. M. Tobias),

[knobloch@px1.berkeley.edu](mailto:knobloch@px1.berkeley.edu) (E. Knobloch),

[mrep@damtp.cam.ac.uk](mailto:mrep@damtp.cam.ac.uk) (M. R. E. Proctor).

the downstream boundary and so takes the form of a wall mode. With increasing forcing the finite amplitude wavetrain fills more and more of the available domain, and once the domain is almost full the wave frequency is determined by the solution of a nonlinear eigenvalue problem. Similar ideas govern the onset of secondary instabilities of the fully developed wavetrain. If noise is present the frequency (and hence wavenumber) selection mechanism is dramatically changed as described in [12]. This phenomenology is believed to be relevant to the onset of dynamo waves in rotating stars [18,19] as well to the process of target wave formation and breakup in reaction-diffusion systems [17], to name but two examples.

The case of Neumann boundary conditions is quite different, however. In this case the Stokes solution remains, and any spatiotemporal chaos present in the BF-stable regime necessarily coexists with this solution. We confirm here that this is indeed the case, and demonstrate that the origin of the chaotic behavior and the associated bistability differs from that familiar from the case of periodic boundary conditions. The results are unexpected, and to us, at least, somewhat surprising.

To understand the origin of the complex behavior in this system we follow through parameter space branches of one and two-frequency states and compute by direct numerical integration states with additional frequencies as well as chaotic states. For this purpose we cannot use the large domains that one would ideally employ, but we believe that our results nonetheless shed considerable light on the behavior in large domains.

We consider the CGL equation with drift in one spatial dimension,

$$A_t + cA_x = \mu A + (1 + i\lambda)A_{xx} - (1 - ia)|A|^2 A, \quad (1)$$

subject to Neumann boundary conditions (NBC):  $A_x(0) = A_x(L) = 0$ . In writing this equation we have removed the oscillation frequency of the basic state with the result that the coefficient  $\mu$ , hereafter the bifurcation parameter, can be taken to be real. The coefficients  $c$ ,  $\lambda$  and  $a$  are also real. The drift term ( $c \neq 0$ ) breaks the left-right symmetry of the equation, and it is the interaction of this symmetry-breaking effect with the downstream boundary at  $x = L$  that is responsible for the behavior described below.

Equation (1) is perhaps the simplest example of a non-normal problem with a stabilizing nonlinearity [7,19]. We are interested in the rôle played by the advection velocity  $c$ , the domain length  $L$  and the bifurcation parameter  $\mu$  for different choices of the parameters  $\lambda$  and  $a$ . The parameters  $c$ ,  $L$  and  $\mu$  are not independent since one of them can be eliminated by rescaling (for example, we may set  $L = 1$  by setting  $\tilde{\mu} = L^2\mu$ ,  $\tilde{c} = Lc$ ,  $\tilde{t} = t/L^2$ ,  $\tilde{x} = x/L$  and  $\tilde{A} = LA$ ) but we prefer to write (1) in the general form (1).

Equation (1) has the trivial solution  $A = 0$  and the spatially uniform (hereafter, flat) Stokes solution

$$A = A_0 e^{i\Omega t}, \quad |A_0| = \sqrt{\mu}, \quad \Omega = \mu a. \quad (2)$$

On an unbounded domain the advection term can be eliminated by writing the equation in the comoving reference frame, and the flat state is then stable with respect to infinitesimal perturbations in the BF-stable regime  $a\lambda < 1$  for all values of  $\mu$  [1,6]. In the case of a large domain with Neumann boundary conditions the advection term cannot be eliminated but the BF stability boundary is only slightly shifted (see below). Thus the basic picture remains unchanged. This BF-stable regime is the focus of the numerical explorations described next.

## 2. Numerical exploration

In this section we present the results of numerical time-stepping of Eq. (1) forwards in time. The parameters are chosen so as to showcase the wide range of dynamic behavior admitted by this simple partial differential equation in a finite domain. We choose  $\lambda = 0.45$  and select the parameter  $a$  such that  $a\lambda < 1$  so that the flat solution is linearly stable for all values of  $\mu$  (and of  $c$ ) in both finite and unbounded domains, and there is a range of initial conditions for which trajectories are attracted to this state. As with a periodic domain, in a finite domain the flat solution is not always a global attractor. We find that there is a range of values of  $\mu$ , i.e. there are  $\mu_1$  and  $\mu_2$  with  $\mu_1 < \mu < \mu_2$ , depending on  $c$  and  $L$ , in which the flat solution coexists with various *stable* nonflat (hereafter, structured) solutions, as described below. The precise nature of the observed dynamics depends sensitively on the choice of parameters, but the observed bistability is robust and occurs for a wide range of parameters. An example is shown in Fig. 1(a) which summarizes our results in the form of a bifurcation diagram for  $\lambda = 0.45$ ,  $a = 2.0$  and  $c = 1.0$ . The figure shows both the flat and the coexisting structured solutions in terms of  $\langle A \rangle_{\max}$ , the successive local maxima (in time) of the average amplitude  $\langle A \rangle \equiv \sqrt{\int_0^L |A(x,t)|^2 dx}/L$ , as a function of  $\mu$  when  $L = 60.0$ . Thus for the flat solution  $\langle A \rangle_{\max} = \sqrt{\mu}$ , while for the structured solution a finite number of values of  $\langle A \rangle_{\max}$  at a given value of  $\mu$  indicates that the solution is temporally quasiperiodic (or periodic); a continuous interval of  $\langle A \rangle_{\max}$  values indicates a chaotic state. Evidently the structured solution undergoes many complicated transitions from stable periodic to quasiperiodic to chaotic dynamics and back again as  $\mu$  varies. A close-up of the transitions near  $\mu = \mu_1 \approx 0.658$  is shown in Fig. 1(b).

Figure 2(a) shows the corresponding bifurcation diagram for  $c = 1.5$ , indicating that  $\mu_1$  and  $\mu_2$  both increase with  $c$  as does the width of the interval  $\mu_2 - \mu_1$  within which bistability occurs:  $\mu_1 = 0.658 < \mu < \mu_2 = 1.53$  for  $c = 1.0$ , and  $\mu_1 = 1.47 < \mu < \mu_2 = 3.61$  for  $c = 1.5$ . Figure 2(b) shows the bifurcation diagram for the complementary problem in which  $\mu$  is held fixed (at  $\mu = 1.5$ ) and  $c$  is varied. The figure indicates that there is again an interval,  $0 < c_1 < c < c_2$ , in which a stable structured state coexists with the flat state, and that the transitions between stable quasiperiodic and chaotic structured states occur along curves in the  $(\mu, c)$

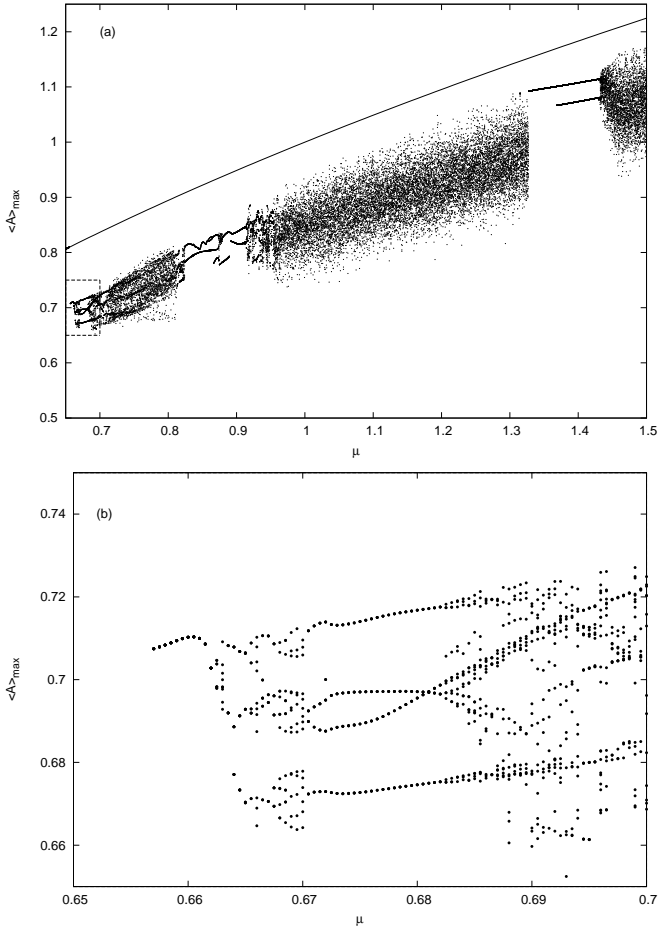


Fig. 1. (a) Bifurcation diagram for solutions of Eq. (1) with  $c = 1.0$ ,  $\lambda = 0.45$ ,  $a = 2.0$  in a domain of length  $L = 60.0$ , showing that for  $0.658 \lesssim \mu \lesssim 1.53$  stable structured solutions coexist with the flat solution  $|A| = \sqrt{\mu}$  (solid line). (b) A close-up of the transitions that occur in the interval  $0.658 \lesssim \mu \lesssim 0.7$  just after the first appearance of stable structured solutions.

plane (for fixed  $L$ ). This behavior is in contrast to the corresponding problem with periodic boundary conditions and no imposed drift ( $c = 0$ ) in which persistent defect chaos is present [1,4]. Thus the use of Neumann boundary conditions in place of periodic boundary conditions suppresses defect chaos provided that  $c < c_1$ . However, the decay of the chaotic state into the competing flat oscillatory state may be exceedingly slow: in domains of size  $L = 60$  the transient chaos may last for several thousand time-units. We surmise that the maintenance of the defect chaos state present with periodic boundary conditions depends sensitively on the cycling of disturbances through the domain, something that cannot take place with Neumann boundary conditions.

We now comment on the nature of the structured state, and the transitions that occur as  $\mu$  is varied. Figure 3 shows two different space-time representations of the stable structured solution when  $c = 1.0$  and  $\mu = 1.4$ . For these parameter values the overall time-dependence of the average root-mean-square of the amplitude is quasiperiodic, as implied by Fig. 1. The real part of  $A(x, t)$  (Fig. 3(a)) shows

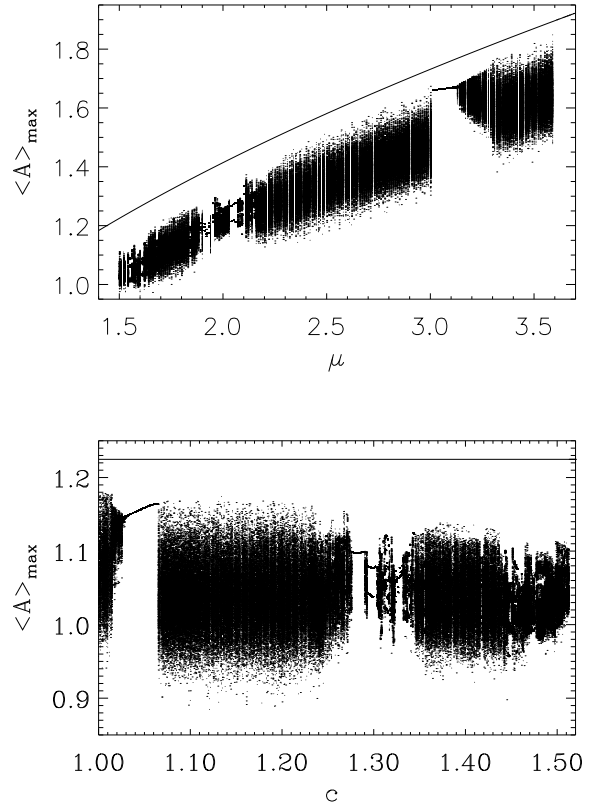


Fig. 2. (a) As for Fig. 1, but with  $c = 1.5$ . The structured state now coexists with the flat solution in the range  $1.47 \lesssim \mu \lesssim 3.61$ . (b) The corresponding bifurcation diagram for  $\mu = 1.5$  with  $c$  as the control parameter. The structured state coexists with the flat state in the range  $0.97 \lesssim c \lesssim 1.513$ .

that the solution consists of a regular sequence of  $\pi$  phase jumps propagating towards the right. These phase jumps are separated from the left boundary by a more-or-less stationary source. The nucleation of the phase jumps near  $x = 0$  occurs periodically with a well-defined period as revealed by the space-time plot of  $|A|$  in Fig. 3(b). Figure 4 shows analogous space-time plots for several additional values of  $\mu$  to show the nature of the transitions that can occur. These plots reveal that the solution can break up into several disjoint states with different properties (wavelength, frequency, amplitude) separated by more-or-less stationary fronts defined by the location of repeated phase slips. These solutions form as a result of several successive absolute secondary instabilities, each of which is responsible for the introduction of a new front into the structure of the solution, as described in [19] for the case of Dirichlet boundary conditions. These fronts usually appear at the right boundary (although this depends on the sign of the group velocity associated with the secondary instability) and, with increasing  $\mu$ , move towards the left. Each secondary instability selects a new frequency which in turn selects the wavenumber and amplitude downstream. If the parameters are such that the selected wavenumbers are

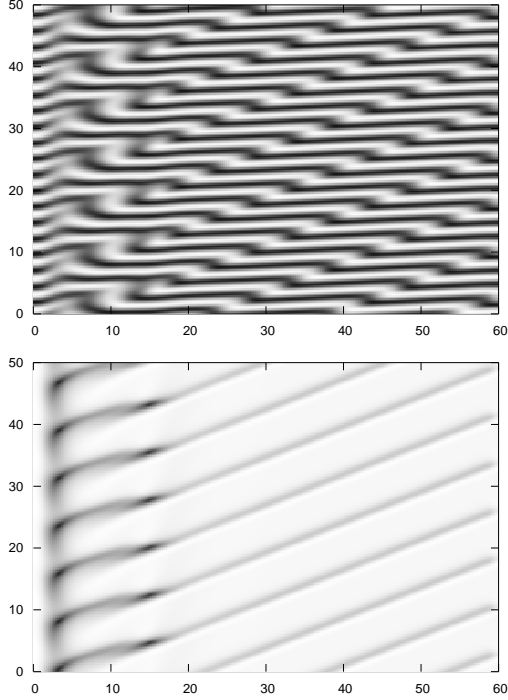


Fig. 3. Space-time representation of the structured state when  $\mu = 1.4$ ,  $c = 1.0$ , with  $x$  ( $0 \leq x \leq 60.0$ ) increasing from left to right, and  $t$  increasing upwards for 50 time units. The panels show  $\text{Re}A$  (upper panel) and  $|A|$  (lower panel), and reveal a periodic sequence of phase jumps propagating in the advection direction (i.e., to the right).

roughly commensurate with the domain length the resulting solution can settle down (via nonlinear frequency adjustment) to a state in which the phase slips occur periodically (or are absent altogether). Such states are periodic in time. Examples of solutions with two fronts are shown in Figs. 4(b,c). Each shows a state where the amplitude near the left boundary oscillates with frequency  $m\Omega$ , in the middle with frequency  $n\Omega$ , and near the right boundary with frequency  $\Omega$  ( $m \geq n \geq 1$ ), as shown in Fig. 5. The whole solution is therefore periodic, but the different spatial regions do not necessarily reveal the correct overall frequency. If the selected wavenumbers are not close to being commensurate with the domain the phase slips will typically be chaotic and the resulting solution will possess at least one chaotic segment (see Fig. 4(a) for  $\mu = 1.5$ ). Such states are typical of values of  $\mu$  lying between the frequency-locked tongues. The tongues are entered via intermittency and exited either via period-doubling or frequency-unlocking leading to quasiperiodicity. No hysteresis associated with the locking process was detected. Similar coexistence between adjacent laminar and turbulent states has been seen in the CGL equation with Dirichlet boundary conditions [19]. This case, however, does not admit the flat state and does not exhibit bistability.

The transitions between the quasiperiodic and chaotic structured solutions can be studied by means of appropriate

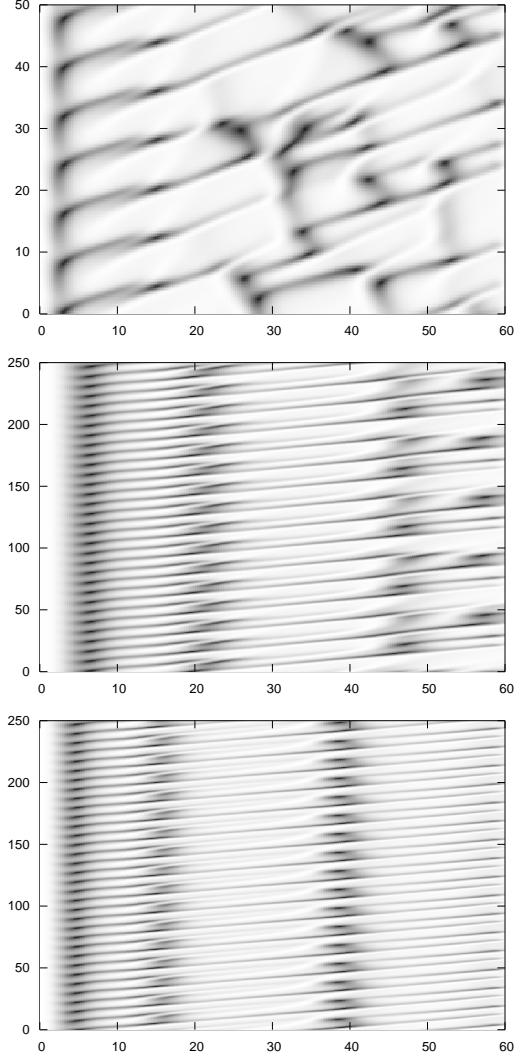


Fig. 4. Space-time representation of the structured state in terms of  $|A|$  when (a)  $\mu = 1.5$ , (b)  $\mu = 0.7$ , (c)  $\mu = 0.9$ , and  $c = 1.0$ ,  $L = 60.0$ . Panel (a) is plotted on the same scale as Fig. 3(b), and reveals phase jumps that propagate rightwards in a chaotic manner. In (b) and (c) the solutions consist of three regions separated by two fronts, with the oscillation frequencies in the three regions linked via integer multiples; in these panels time increases upwards for 250 time units.

Poincaré sections. For this purpose we let  $A_r$  be the value of  $A$  at the right side of the domain ( $x = L$ ), and plot  $\text{Re}A_r$  versus  $\text{Im}A_r$  at a fixed value of  $|A_r|$ . Figure 6(a) shows the resulting section for  $\mu = 1.4$  while Fig. 6(b) shows the result for  $\mu = 1.5$ . For  $\mu = 1.4$  the amplitude  $|A_r|$  is periodic in time as suggested by the space-time plot in Fig. 3, and the Poincaré section takes the form of two invariant circles very close together. In contrast, at  $\mu = 1.5$  the solution is chaotic (see Fig. 4(a)) and the Poincaré section indicates that the torus has broken down.

It is evident that, for a large range of parameters, a stable flat state coexists with structured states that undergo many transitions as the parameters are varied. In the next two sections, we explore the origin of the observed behavior

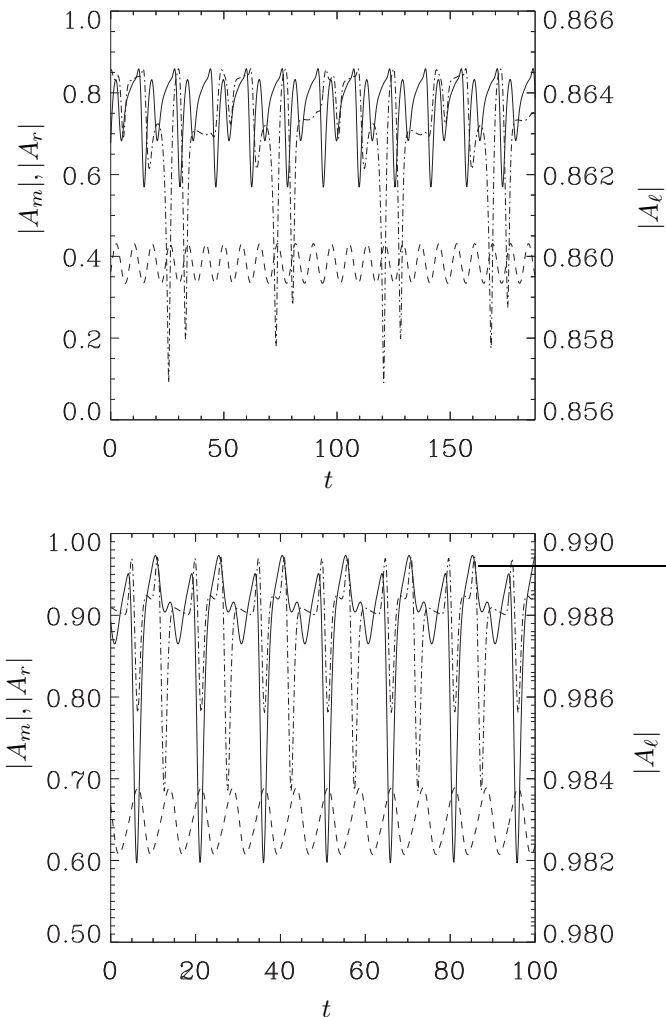


Fig. 5. Time series for  $|A_\ell| \equiv |A(x=0)|$  (dashed line),  $|A_m| \equiv |A(x=L/2)|$  (solid line) and  $|A_r| \equiv |A(x=L)|$  (dashed-dotted line) for the resonant solutions shown in Figs. 4(b,c), respectively. In (a) the frequencies are in the ratio 12 : 6 : 1 while in (b) they are in the ratio 2 : 1 : 1.

and its relation to the corresponding behavior present in unbounded domains.

### 3. Theory

In this section we explore the possibility that the structured states that coexist with the flat state in the BF-stable regime are the result of a ‘bifurcation from infinity’ [5,13] much as occurs, for example, in pipe flow which is linearly stable for all values of the Reynolds number and yet admits ‘turbulent’ states arising from finite amplitude perturbations [8,11]. In particular, we explore the possibility that in the BF-unstable case these states originate in the Benjamin-Feir instability of the flat state. If this is the case the BF instability is expected to be subcritical, and the key to understanding the origin of bistability in the BF-stable regime is provided by the passage through the stability boundary  $a\lambda = 1$ . The results presented below support certain aspects of this picture, but not all of it.

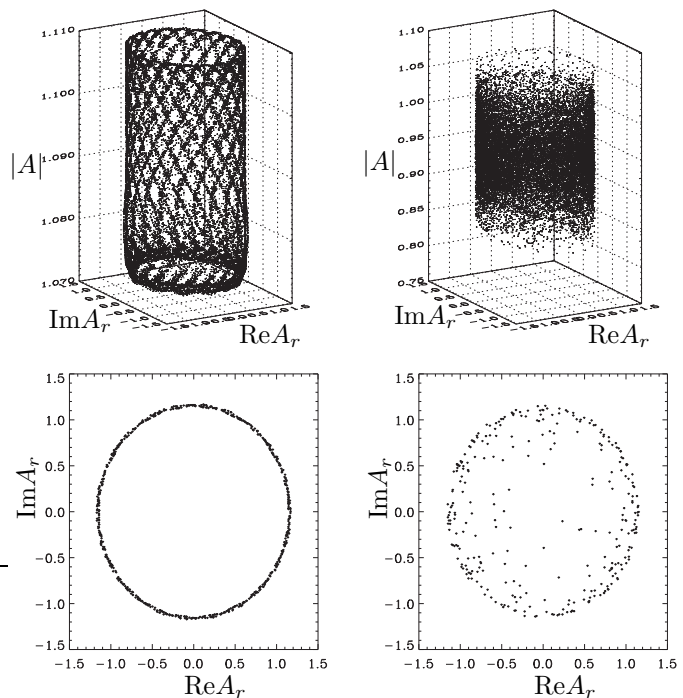


Fig. 6. Transition from quasiperiodic to chaotic behavior when  $L = 60.0$ . (a)  $\mu = 1.4$ ,  $|A_r| = 1.09$  (quasiperiodic), (b)  $\mu = 1.5$ ,  $|A_r| = 0.95$  (chaotic).

#### 3.1. Linear theory

The linear stability properties of the flat state in an unbounded domain are well understood. This is not so, however, in a finite domain. In order to determine the linear stability of the flat state we write

$$A(x, t) = A_0 e^{i\Omega t} \left( 1 + \alpha_1(x) e^{st} + \alpha_{-1}(x) e^{s^* t} \right), \quad (3)$$

where  $s = \sigma + i\omega$  is the complex growth rate, and  $s^*$  is the complex conjugate of  $s$ . Substitution into Eq. (1) followed by linearization yields the system

$$\begin{aligned} s\alpha_1 &= -\mu(1-ia)(\alpha_1 + \alpha_{-1}^*) - c\alpha_1' + (1+i\lambda)\alpha_1'' \quad (4) \\ s^*\alpha_{-1} &= -\mu(1-ia)(\alpha_{-1} + \alpha_1^*) - c\alpha_{-1}' + (1+i\lambda)\alpha_{-1}'' \quad (5) \end{aligned}$$

with  $\alpha_{\pm 1}' = 0$  at  $x = 0, L$ . We solve this boundary value problem using the Newton-Raphson-Kantorovich algorithm (NRK) [3], searching for states with  $\text{Re } s = \sigma = 0$ . There are two possibilities: either  $\text{Im } s = 0$  or  $\text{Im } s \neq 0$ , corresponding, respectively, to a steady state and a Hopf bifurcation. Once found, the marginally stable eigensolution can be continued in the parameter  $a$  (with  $\lambda$  fixed) to map out the complete linear stability boundary. The resulting boundary is shown in Fig. 7 for two values of  $c$ . In Fig. 7(a) the flat solution loses stability as  $\mu$  increases through  $\mu = \mu_c$  via a Hopf bifurcation, producing quasiperiodic states. Figure 7(b) shows that for smaller values of  $c$  and  $a > a_{min}$  the flat state loses stability via a steady state bifurcation as  $\mu$  increases ( $a_{min} = 2.36$  for the case shown in the figure). For intermediate values of  $a$  the flat state restabilizes with increasing  $\mu$  before losing stabil-

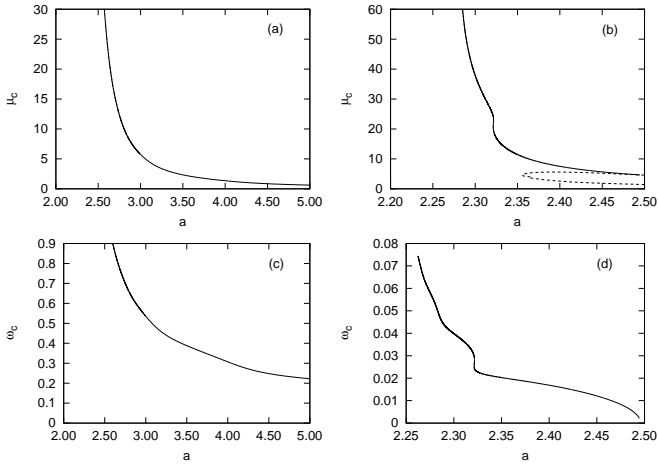


Fig. 7. Variation of  $\mu_c$  and  $\omega_c$  with  $a$  for (a,c)  $c = 0.5$  and (b,d)  $c = 0.05$ . Solid (broken) lines indicate Hopf (steady state) bifurcations. Parameters:  $L = 6.0$  and  $\lambda = 0.45$ .

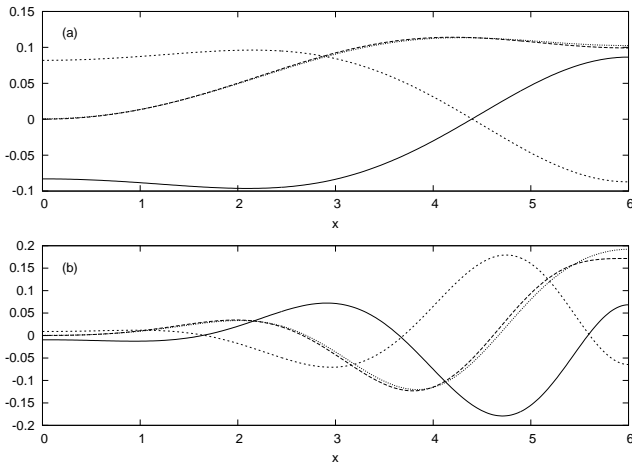


Fig. 8. Eigenfunctions for (a)  $c = 0.05$  ( $a = 2.35$ ), (b)  $c = 0.5$  ( $a = 2.70$ ). Real (imaginary) part of  $\alpha_1$  is indicated by solid (dashed) lines; real (imaginary) part of  $\alpha_{-1}$  is indicated by short-dashed (dotted) lines. In (a) the imaginary parts of  $\alpha_1$  and  $\alpha_{-1}$  are almost identical with differences only apparent near  $x = 6$ . This similarity is due to  $c$  being small.

ity again at a Hopf bifurcation. However, for larger values of  $a$  ( $a > 2.5$  in Fig. 7(b)) a second real eigenvalue becomes unstable with increasing  $\mu$  and these eigenvalues then collide on the positive real axis, move into the complex plane but remain unstable. Thus for  $a > 2.5$  the restabilization region is absent. Additional eigenvalues becomes unstable for larger  $a$  and/or  $\mu$ . Typical eigenfunctions are shown in Fig. 8.

In the absence of the drift term ( $c = 0$ ) the linear stability problem can be solved analytically. All bifurcations are steady state and occur at

$$\mu_n = \frac{n^2 \pi^2 (1 + \lambda^2)}{2L^2 (a\lambda - 1)}, \quad (6)$$

where  $n = 1, \dots$  is an integer; the corresponding eigenfunctions are  $\alpha_{\pm 1} \sim \cos(n\pi x/L)$ . Thus for large  $L$  and  $a\lambda > 1$  the secondary instability occurs close to the primary bi-

furcation at  $\mu = 0$  that produces the flat state. As  $a\lambda - 1$  decreases towards zero for fixed  $L$  the instability threshold increases without bound and for  $a\lambda < 1$  no instability is present. In contrast, when  $c \neq 0$  the threshold  $\mu_c$  for the first Hopf mode appears to diverge as  $(a\lambda - 1)^{-2}$ .

In the following we refer to the case  $\mu_c < \infty$  as BF-unstable; otherwise the flat state is BF-stable.

### 3.2. Nonlinear quasiperiodic states

In general, numerical tracking of quasiperiodic (hereafter, QP) states presents a difficult problem [14,15], particularly in partial differential equations. To make progress we limit the domain size to  $L = 6.0$  and decompose the QP solutions that bifurcate from the flat state in the BF-unstable regime into temporal harmonics:

$$A(x, t) = A_0 e^{i\Omega t} \sum_{-\infty}^{\infty} \alpha_n(x) e^{in\omega t}. \quad (7)$$

The functions  $\alpha_n$  then obey the coupled equations

$$i\Omega \alpha_n + in\omega \alpha_n = \mu \alpha_n - c \alpha_n' + (1 + i\lambda) \alpha_n'' - \mu (1 - ia) \sum_{p,q,r} \alpha_p \alpha_q^* \alpha_r \delta_{p-q+r,n}, \quad (8)$$

where  $\omega$  and  $\Omega$  are regarded as eigenvalues, of a nonlinear eigenvalue problem, that must be determined as part of the solution. Both are, of course, known at the point of bifurcation. The presence of two eigenvalues is a consequence of the presence of two undetermined phases in a QP solution; we fix these phases by choosing the overall phase of the  $\alpha_n$ 's, i.e., the phase of  $A_0$ , and the origin of time. As a global diagnostic for this state, we compute the time-averaged squared amplitude given by

$$\mathcal{A}^2 = \frac{\mu}{L} \sum_{-\infty}^{\infty} \int_0^L |\alpha_n|^2 dx. \quad (9)$$

For the flat oscillatory state,  $\alpha_0 = 1$  and  $\alpha_n = 0$  for  $n \neq 0$ , and so  $\mathcal{A}^2 = \mu$ . For comparison with the time-stepping results we also calculate  $\langle A \rangle_{max}$  as previously defined.

In order to make progress numerically we must truncate the summation in Eq. (7). The results presented below have been computed at a truncation level of 4, i.e., for 9 complex modes  $\alpha_{-4}, \alpha_{-3}, \dots, \alpha_4$ . Further calculations have been carried out at a truncation level of 8 (17 complex modes) and found to show no significant variation from the results presented below.

In Fig. 9 we show examples of continuation from the first Hopf (more precisely, torus) bifurcation on the flat state for two different values of  $c$  with  $a = 3$  and  $L = 6.0$ . The bifurcation points are indicated by filled circles. The figure demonstrates that, as hypothesized, the bifurcation is subcritical, and hence that the QP branch is initially unstable. This property of the system is shared by all parameter values investigated. As we move away from the bifurcation point the frequency  $\omega$  changes significantly, while  $\Omega$  changes

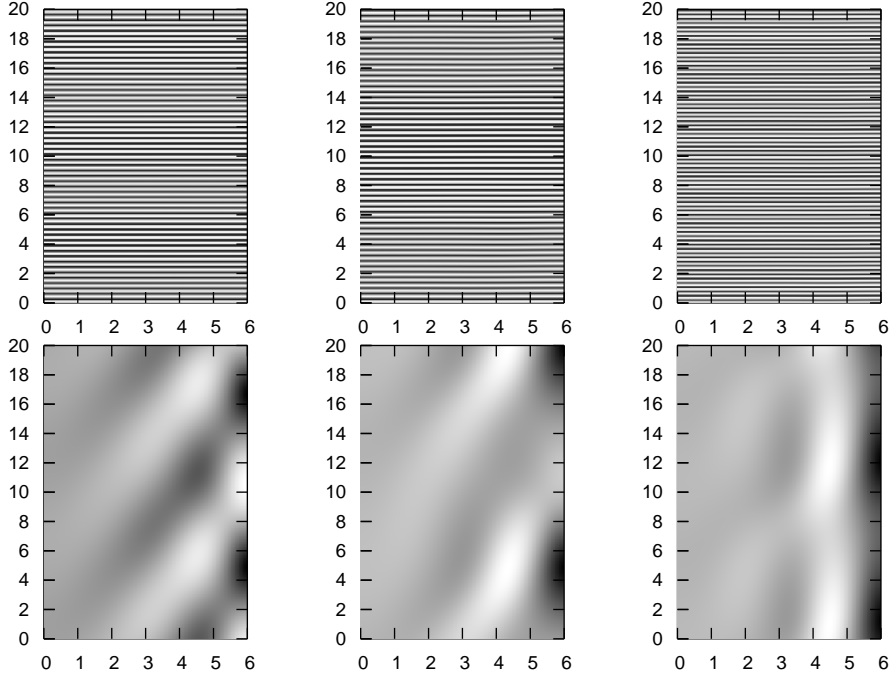


Fig. 10.  $\text{Re}A$  (upper panels) and  $|A|$  (lower panels) for the quasiperiodic solutions for  $\lambda = 0.45$ ,  $a = 3.0$ ,  $L = 6.0$ ,  $c = 0.5$  and three values of  $\mu$ . From left to right:  $\mu = 5.73$  ( $\omega = 0.53$ , near onset),  $\mu = 5.64$  ( $\omega = 0.42$ ),  $\mu = 7.22$  ( $\omega = 0.58$ ).

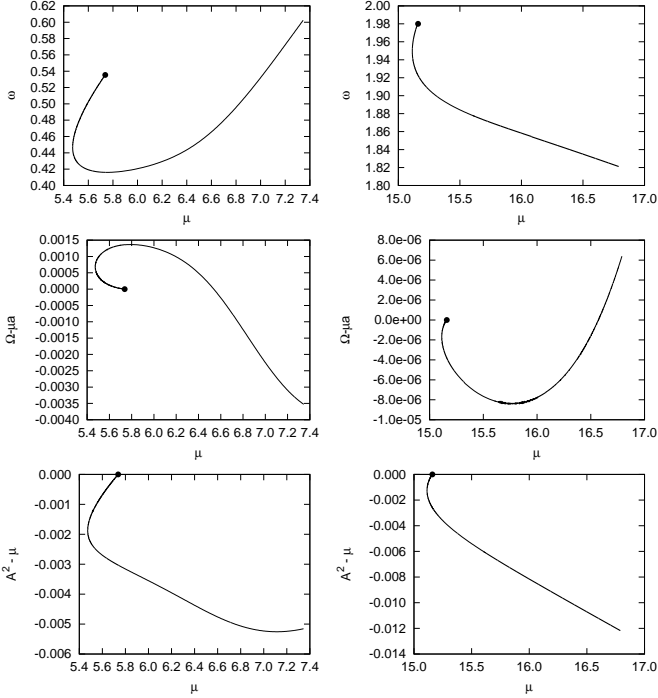


Fig. 9. The two frequencies  $\omega$ ,  $\Omega - \mu a$  along the QP branch together with the relative squared amplitude  $\mathcal{A}^2 - \mu$ , as functions of  $\mu$  for  $\lambda = 0.45$ ,  $a = 3.0$ ,  $L = 6.0$  and  $c = 0.5$  (left column),  $c = 1.0$  (right column). The location of the initial Hopf (torus) bifurcation is marked with a filled circle. In both cases the branch appears to terminate with increasing  $\mu$ .

scarcely at all. This is so for both  $c = 0.5$  and  $c = 1.0$  despite the different  $\mu$  dependence. In addition, Figs. 9(c,f) show that the amplitude  $\mathcal{A}$  of the quasiperiodic state is al-

Mode $n$	$E_n = L^{-1} \int_0^L  \alpha_n ^2 dx$
$\alpha_{-2}$	$3.21 \times 10^{-6}$
$\alpha_{-1}$	$6.01 \times 10^{-4}$
$\alpha_0$	$9.98 \times 10^{-1}$
$\alpha_1$	$5.85 \times 10^{-4}$
$\alpha_2$	$3.98 \times 10^{-6}$

Table 1  
'Energy'  $E_n$  in the dominant modes at  $\mu = 16.78$  on the QP branch near the breakdown of the continuation procedure. In practice  $E_n$  is computed as the sum of the squares of each mode at each of the 1024 gridpoints used.

ways less than that of the corresponding flat state, albeit by a very small amount. This observation is reinforced by the space-time plots shown in Fig. 10 for  $c = 0.5$ . These reveal the changes that take place in the quasiperiodic state as one follows the branch from the initial Hopf bifurcation. The upper panels ( $\text{Re} A$ ) show that the oscillation is strongly dominated by the spatially uniform component with oscillation frequency  $\Omega$ . This frequency is eliminated in the lower panels which show  $|A|$  and reveal the additional spatial and temporal structure of the quasiperiodic states. As expected, this structure is concentrated near the upstream boundary.

To confirm the visual impression from these space-time plots we list in Table 1 the energy in the various frequency components far from the initial Hopf bifurcation when  $c = 1.0$ . It is evident that the oscillation is dominated by a large margin by the  $\alpha_0$  component.

Attempts to continue the QP solutions, using the parameter  $a$ , into the BF-stable region ( $a\lambda < 1$ ) proved unsuccessful. In practice it has not been possible to decrease  $a$

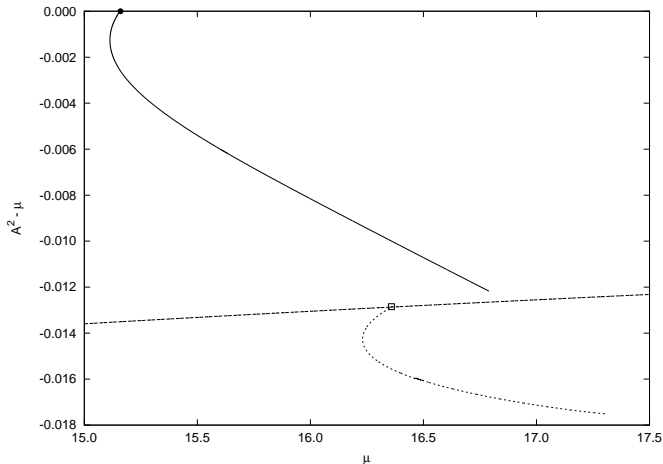


Fig. 11. High resolution continuation of the QP branch bifurcating from the flat state (solid line) and of the single-frequency spatially structured state (dashed line) for  $c = 1.0$ . A Hopf (torus) bifurcation (open square) on the latter generates a distinct QP branch (dotted line).

(at fixed  $\mu$ ) by more than a couple of percent before the solution undergoes a saddle-node bifurcation and  $a$  must be increased once again to remain on the solution branch. However, despite this difficulty we expect that, for large enough  $\mu$ , subcritical branches exist that extend into the BF-stable regime.

### 3.3. Single-frequency spatially structured states

Figure 11 explores the termination of the QP branch shown in Fig. 9(f). The figure shows that the branch approaches close to a branch of (unstable) single-frequency spatially structured states (dashed line), and identifies a Hopf (torus) bifurcation (open square) on this branch. However, the QP branch (dotted line) that bifurcates from this point remains distinct, and despite much effort neither QP branch could be followed beyond the values of  $\mu$  shown. Figures 12(a,b) show the two frequencies,  $\omega$  and  $\Omega$ , along the two QP branches; Fig. 12(b) also shows the frequency  $\Omega$  along the branch of single-frequency structured states (dashed line). Further Hopf (torus) bifurcations on the spatially structured single-frequency branch occur at larger values of  $\mu$  but are not candidates for the termination of either QP branch.

In the remainder of this section we explore the properties of the single-frequency spatially structured states revealed in Fig. 11. These can be continued towards smaller values of  $\mu$ , where they undergo a saddle-node bifurcation, acquire stability, and turn back towards larger  $\mu$  along a ‘lower’ branch (Fig. 13). Time-stepping results confirm the initial stability of the lower branch and identify a supercritical Hopf (torus) bifurcation on this branch that leads to a *stable* QP branch with increasing  $\mu$ , also shown in Fig. 13. The behavior of the frequencies  $\omega$  and  $\Omega$  along this branch is shown in Fig. 14. With increasing  $\mu$  the QP branch undergoes further transitions producing multi-frequency or

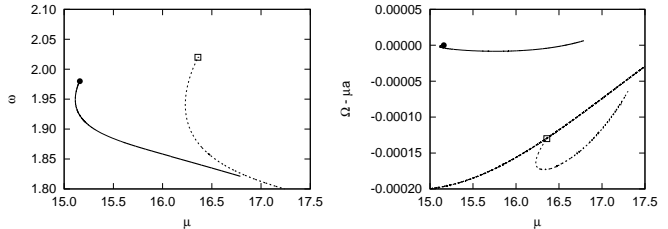


Fig. 12. The frequencies (a)  $\omega$  and (b)  $\Omega$  as a function of  $\mu$  on the QP branch from the flat state (solid line) and on the QP branch from the structured state (dotted line). Fig. (b) also shows the frequency  $\Omega$  of the single-frequency structured states (dashed line). The Hopf bifurcation on the latter is indicated by an open square.

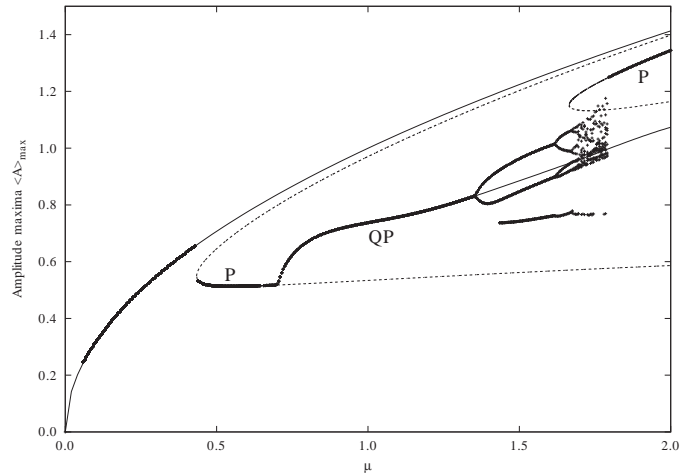


Fig. 13. Bifurcation diagram for  $\lambda = 0.45$ ,  $a = 3.0$ ,  $L = 6.0$ ,  $c = 1.0$ . Both single-frequency (labeled P) and two-frequency (labeled QP) states have been obtained using continuation. Thin solid (dashed) lines indicate stable (unstable) solutions. Superposed time-stepping results (+) confirm stability assignments from continuation, and reveal additional multi-frequency and chaotic states.

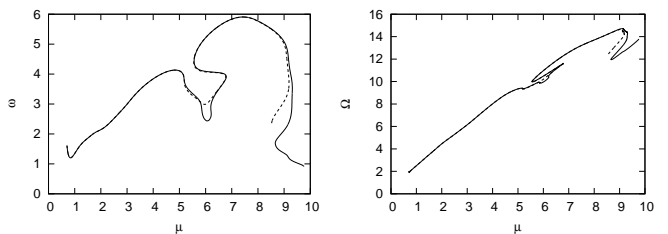


Fig. 14. The frequencies  $\omega$  and  $\Omega$  along the QP branch in Fig. 13. The solid line has a truncation level  $N = 6$ , while the dashed line has  $N = 4$ . Agreement is excellent for  $\mu \lesssim 5.0$ .

chaotic states before eventually losing stability and collapsing onto a new branch of single-frequency spatially structured states (Fig. 13). In Figs. 15 and 16 we show a three-frequency state at  $\mu = 1.5$  and a chaotic state at  $\mu = 1.79$ , respectively, both in the form of space-time plots. The transition from these states to the new single-frequency state is hysteretic, and its complexity appears to be the result of the breakdown of the three-torus as it approaches an unstable single-frequency state (dashed line in Fig. 13).

In Fig. 17 we show an unstable two-frequency solution at  $\mu = 1.5$  obtained by numerical continuation from the

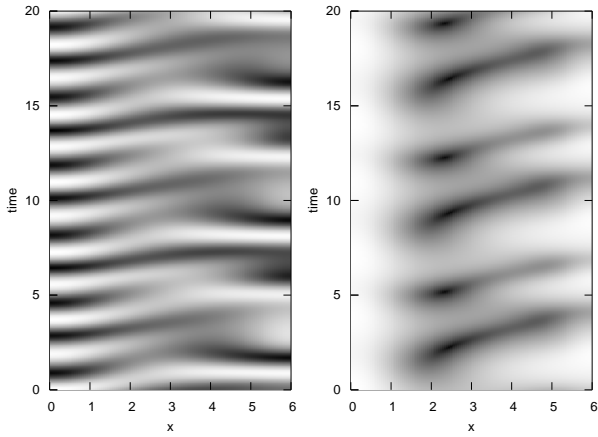


Fig. 15. A stable three-frequency solution in terms of  $\text{Re}A$  (left panel) and  $|A|$  (right panel) obtained by time-stepping at  $\mu = 1.5$  in Fig. 13.

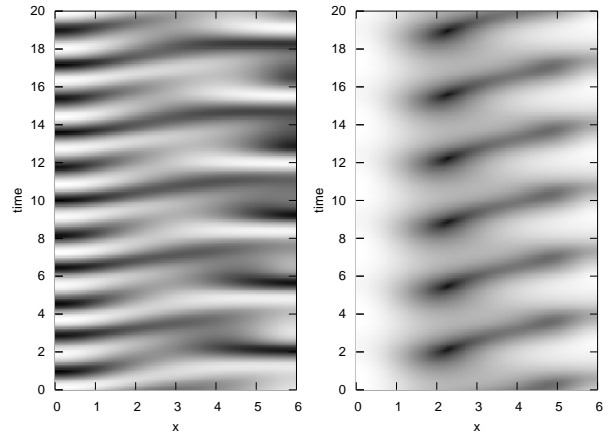


Fig. 17. An unstable two-frequency quasiperiodic solution at  $\mu = 1.5$  (Fig. 13) obtained by continuation, in terms of  $\text{Re}A$  (left panel) and  $|A|$  (right panel).

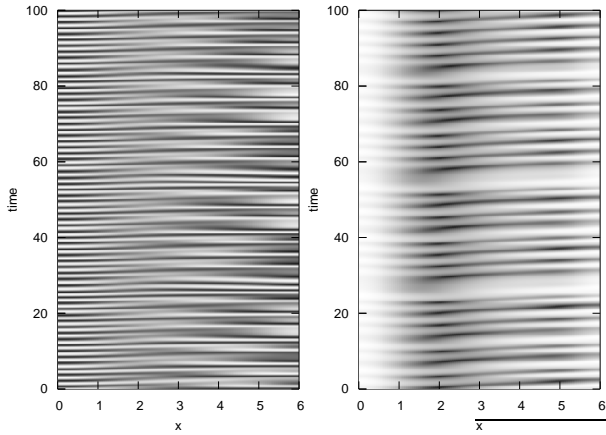


Fig. 16. As in Fig. 15 but for  $\mu = 1.79$ . This value is just below the transition to a new single-frequency spatially structured state as  $\mu$  increases.

single-frequency spatially structured state. Figure 13 shows that this state is unstable to the three-frequency state shown in Fig. 15. The numerical procedure in this case is much less delicate than in the case of the Benjamin-Feir bifurcation from the flat oscillatory state, partly because the QP state is initially stable, and partly as a result of the nontrivial spatial structure of this state. Indeed, it appears that the numerical difficulties in the former case arise from the degeneracy of the flat state for the given boundary conditions. The quasiperiodic states obtained agree precisely with the time-stepping results (Fig. 13), from the initial Hopf bifurcation right up to the loss of stability to the three-frequency states provided only that a sufficient number of modes is included.

In Fig. 18 we indicate how the known branches fit together in the Benjamin-Feir unstable regime with  $c = 1.0$ . Hopf and saddle-node bifurcations are indicated by filled and empty circles, respectively.

Unlike the QP states that bifurcate from the flat oscillatory state, the single-frequency spatially structured state

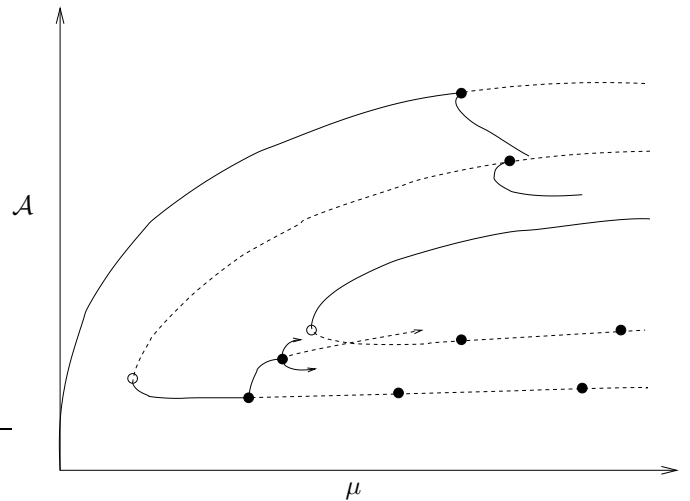


Fig. 18. Sketch of the solutions branches in the Benjamin-Feir unstable regime. Solid (dashed) lines indicate stable (unstable) branches; filled (empty) circles indicate Hopf (saddle-node) bifurcations. The figure includes two QP branches, one that bifurcates from the (upper) flat state, and one that consists of structured states (with arrow). The stability properties of the former are not known.

has been successfully tracked into the Benjamin-Feir stable region ( $a = 2.0$ ,  $a\lambda = 0.9 < 1$ ). The corresponding bifurcation diagram can then be recomputed starting from this state using numerical continuation. The result is shown in Fig. 19. It is evident that the QP branch computed this way agrees almost exactly with the time-stepping results provided the QP solutions are stable. This is no longer the case beyond  $\mu \approx 1.8$ , where the QP branch (found by continuation) undergoes a saddle-node bifurcation. This feature of the diagram may change if more modes ( $N > 6$ ) are included in the truncation. No evidence of the multi-frequency states present in the BF-unstable regime has been found in this regime. A typical solution is shown in Fig. 20 in a space-time plot.

Comparison between Figs. 13 and 19 suggests that the two single-frequency spatially structured states have col-

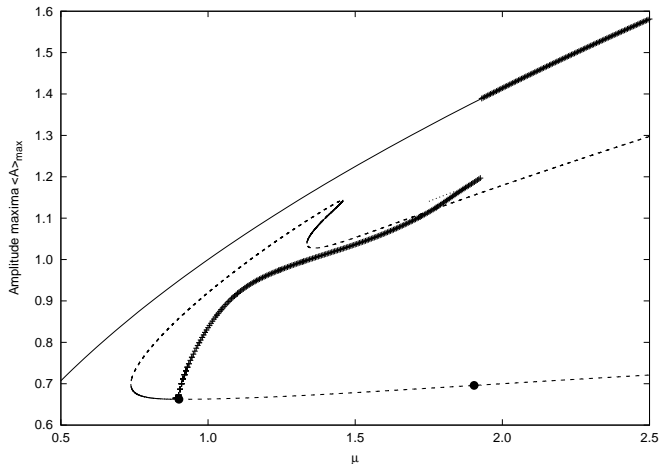


Fig. 19. Bifurcation diagram in the Benjamin-Feir stable regime ( $\lambda = 0.45$ ,  $a = 2.0$ ) for  $c = 1.0$  in a  $L = 6.0$  domain. The upper curve represents the flat oscillatory state while the lower curve shows single-frequency spatially structured states. Solid (dashed) lines indicate stable (unstable) branches. Hopf bifurcations are shown using filled circles. The QP branch obtained via numerical continuation (dots) agrees with the time-stepping results (+’s) right up to the saddle-node at  $\mu \approx 1.93$ . With further increase in  $\mu$  the time-stepping results collapse onto the stable flat state, resulting in hysteresis between the flat state and the QP branch.

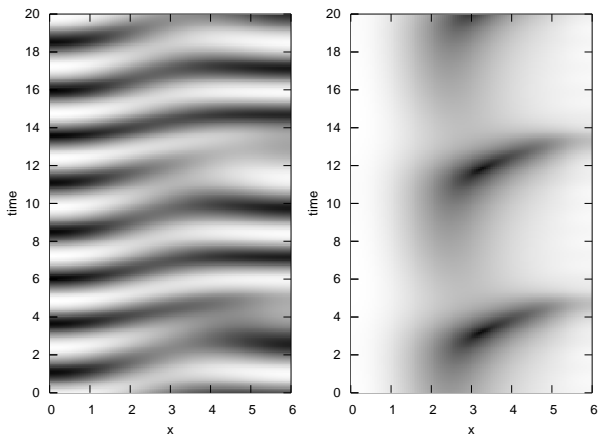


Fig. 20. A stable quasiperiodic solution in the Benjamin-Feir stable region ( $\lambda = 0.45$ ,  $a = 2.0$ ) for  $\mu = 1.5$ ,  $c = 1.0$ ,  $L = 6.0$  in terms of  $\text{Re}A$  (left panel) and  $|A|$  (right panel).

lided and pinched off, creating the small stable section (around  $\mu = 1.4$  with  $\mathcal{A} = 1.1$ ). A second, disconnected, branch is present at larger  $\mu$  (not shown). However, a direct comparison between Fig. 19 and the results reported in Figs. 1 and 2 obtained by time-stepping in the BF-stable regime is not possible in view of the different domain sizes. For direct comparison, we would need to choose  $c = 10.0$  for the computations in the smaller domain.

#### 4. Solutions bifurcating from the trivial state

In addition to the flat state that bifurcates from the trivial state at  $\mu = 0$  there are spatially structured states that

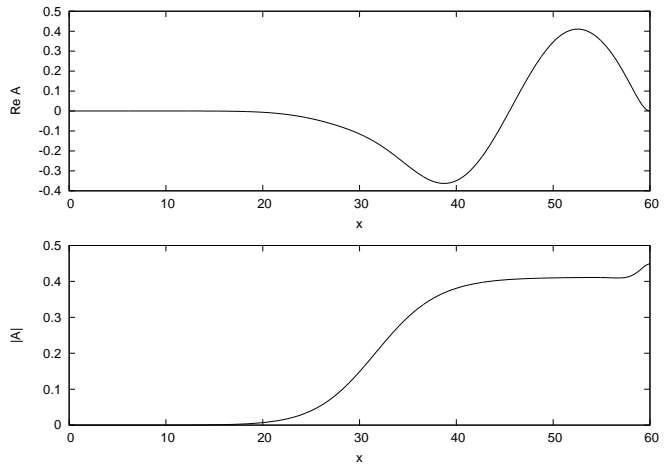


Fig. 21. Unstable periodic solution of Eq. (1) for  $\mu = 0.22$ ,  $\lambda = 0.45$ ,  $a = 2.0$ ,  $c = 1.0$ ,  $L = 60.0$ , showing (a)  $\text{Re}A$  and (b)  $|A|$ . The solution is similar to those for Dirichlet boundary conditions [19], and bifurcates from the trivial solution at the absolute instability boundary.

bifurcate from the trivial state in a sequence of Hopf bifurcations at  $\mu_n = \frac{c^2}{4(1+\lambda^2)} + \frac{\pi^2 n^2}{L^2}$ ,  $n = 1, \dots$  [19]. All of these states are initially unstable, but nonetheless may be followed into the nonlinear regime.

Figure 21 shows what happens when the  $n = 1$  branch is followed in a large domain,  $L = 60.0$ , when  $\lambda = 0.45$ ,  $a = 2.0$ ,  $c = 1.0$ , and  $\mu = 0.22$ ; Fig. 22 shows the corresponding results for  $\mu = 0.5$ . These results resemble those familiar from the corresponding problem with Dirichlet boundary conditions: for small  $\mu$  the solution is confined to the vicinity of the downstream boundary, and spreads upstream with increasing  $\mu$ , exactly as described in [19]. In Fig. 23 we compare the frequencies  $\Omega$  of the solutions of the Neumann and Dirichlet problems as a function of  $\mu$ , again for  $L = 60.0$ . In the small amplitude regime the frequency is insensitive to the exact form of the boundary conditions (as noted in [19]) but at larger values of  $\mu$  the boundary conditions play an important role in determining the frequency, and hence the solution wavenumber.

Figure 24 shows the frequency and amplitude of the corresponding  $n = 1$  states in a smaller domain ( $L = 6.0$ ) but now in the BF-unstable regime ( $\lambda = 0.45$ ,  $a = 3.0$ ). The figure shows that when  $c = 1.5$  the solution spreads out from its initial wall mode structure at  $x = L$  as  $\mu$  increases beyond  $\mu_n$  and invades the upstream domain, much as occurs in the larger domain. In contrast, when  $c = 0.5$  the behavior with increasing  $\mu$  is quite different. Figure 25 shows that the solutions become more and more confined towards the downstream boundary, even as their amplitude increases. This behavior is quite different from that encountered in Figs. 21 and 22 where with increasing  $\mu$  the solutions spread upstream [19]. Evidently when  $a\lambda > 1$  and  $c$  is small the nonlinear effects lead to dynamic “self-focusing” of the solution, in contrast to the case  $a\lambda < 1$  where the focusing effect is due to advection at the drift speed and so is kinematic in nature. However, as shown in Fig. 25(c) these

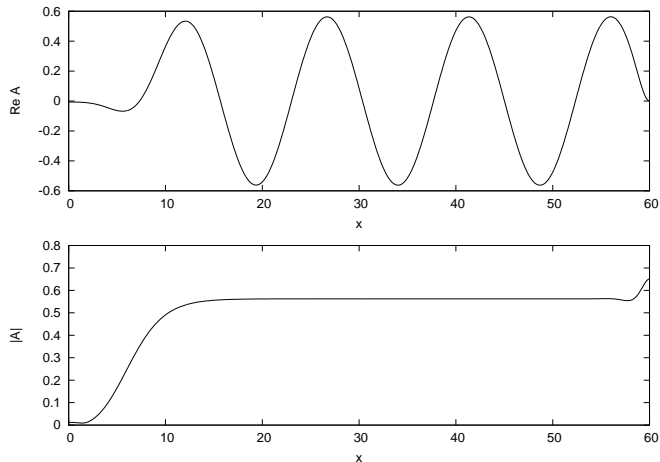


Fig. 22. As for Fig. 21, but for  $\mu = 0.5$ . The solution now fills the domain and its wavelength is shorter.

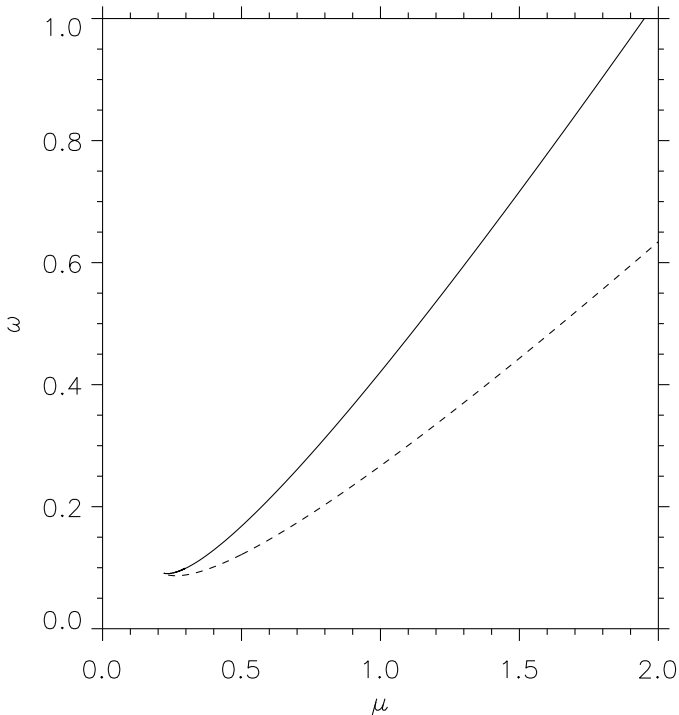


Fig. 23. Frequency dependence of (stable) nonlinear solutions with Dirichlet boundary conditions (dashed line) compared with the (unstable structured) solutions present with Neumann boundary conditions (solid line). In the weakly nonlinear regime the boundary conditions do not affect the frequency, but this is no longer so in the fully nonlinear regime. Parameters:  $\lambda = 0.45$ ,  $a = 2.0$ ,  $c = 1.0$ ,  $L = 60.0$ .

states are destabilized by a succession of Hopf bifurcations. The growth rate of the instability is generally very small, however, and consequently structures of this type can be observed as long-lived features in the time-dependent behavior of the system. This “self-focusing” effect appears to be independent of the choice of boundary conditions and is present even when  $c = 0$ . Figure 26 displays the focusing effect in a larger domain with Dirichlet boundary conditions ( $A(0) = A(L) = 0$ ) and no imposed drift, and demonstrates that the focusing becomes stronger with increasing forc-

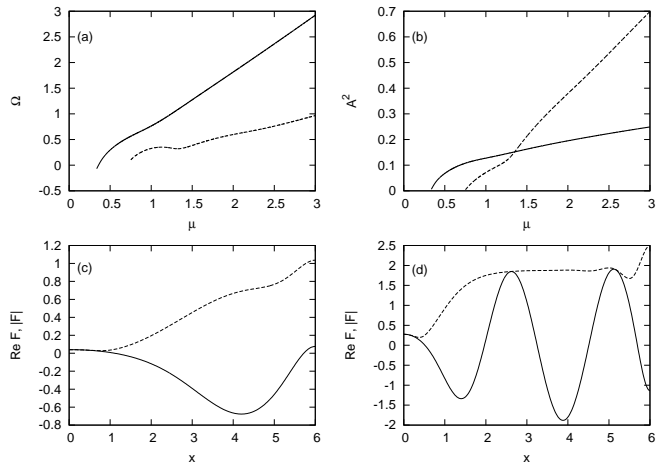


Fig. 24. The  $n = 1$  single-frequency spatially structured state that bifurcates from the trivial state as a function of  $\mu$  for  $c = 0.5$  (solid lines) and  $c = 1.5$  (dashed lines). (a) The frequency  $\Omega$ , (b) the time-averaged square amplitude  $\mathcal{A}^2$ . Panels (c,d) show the nonlinear solutions for  $c = 1.5$  present at  $\mu = 1.75$  and  $\mu = 9.75$ , respectively, in terms of  $\text{Re}F$  (solid lines) and  $|F|$  (dashed lines), where  $A(x, t) = F(x) \exp i\Omega t$ . Parameters:  $\lambda = 0.45$ ,  $a = 3.0$ ,  $L = 6.0$ .

ing, and hence with increasing nonlinearity. Numerically we have been able to follow these states with increasing  $\mu$  into  $\mu > 100$  and find that their maximum amplitude increases as  $\sqrt{\mu}$  while their width decreases as  $1/\sqrt{\mu}$ . In particular, for the parameters of Fig. 26 the maximum amplitude of  $\text{Re}F(x)$  scales as  $0.75\sqrt{\mu}$  while its distance from the upstream boundary scales as  $2.44/\sqrt{\mu}$ . These scalings are characteristic of unbounded domains and suggest that related pulse-like states represent exact solutions of the CGL equation on unbounded domains. We anticipate that these states take the form of a traveling pulse homoclinic to  $A = 0$  by analogy with the *homoclon*s [20] and *modulated amplitude waves* [2] which describe hole-like states homoclinic to  $|A| = \sqrt{\mu}$ , and that the main role of the boundaries is to ‘pin’ these states. If correct this explanation explains why the localized structures are both stationary (albeit time-periodic) and located at one of the boundaries. This conjecture is explored in greater detail in a companion paper.

We now return to the BF-stable regime and examine the bifurcation diagram near onset of the primary instability in greater detail. For this purpose we select a smaller domain ( $L = 6.0$ ) with Neumann boundary conditions and no imposed drift. Figure 27 shows the resulting bifurcation diagram. The primary branch bifurcates from the trivial state at a Hopf bifurcation with a pair of complex conjugate unstable eigenvalues. These collide on the positive real axis at a location indicated by the (first) filled diamond, and with increasing  $\mu$  one of the resulting real eigenvalues passes through the origin into the left half plane, triggering a steady state bifurcation at the location marked by a filled square. This bifurcation is a symmetry-breaking pitchfork bifurcation. The pitchfork produces two solutions, one weakly confined near the left boundary ( $x = 0$ ) and the other weakly confined near the right boundary ( $x = L$ ).

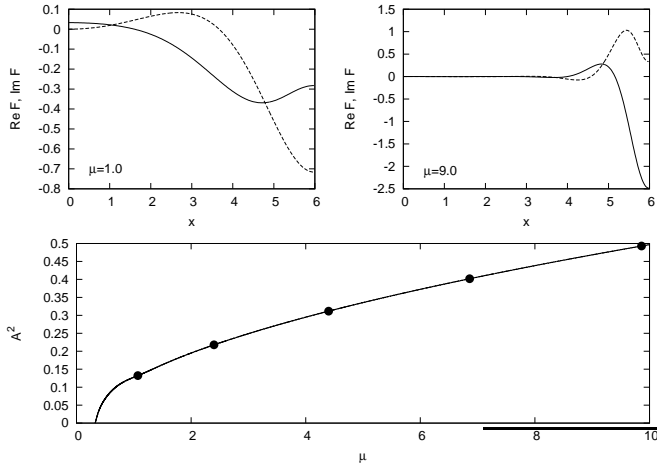


Fig. 25. Continuation of the (unstable) single-frequency spatially structured  $n = 1$  branch. The upper panels show the solution at  $\mu = 1.0$  and  $\mu = 9.0$ , in terms of  $\text{Re}F$  (solid lines) and  $\text{Im}F$  (dashed lines). The lower panel shows the amplitude  $|F|^2$  as a function of  $\mu$ , cf. Fig. 24(b). Subsequent Hopf bifurcations are shown using filled circles. Parameters:  $\lambda = 0.45$ ,  $a = 3.0$ ,  $c = 0.5$ ,  $L = 6.0$ .

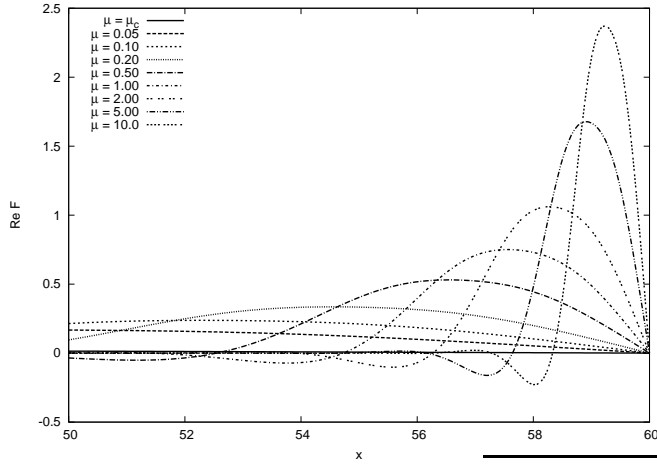


Fig. 26.  $\text{Re}F$  near  $x = 60.0$  for Dirichlet boundary conditions and various values of  $\mu$  with no imposed drift. Only a fraction of the domain is shown since the states are localized near the boundary. Parameters:  $\lambda = 0.45$ ,  $a = 3.0$ ,  $c = 0$ ,  $L = 60.0$ .

These states inherit the remaining unstable eigenvalue in the positive half plane and so are initially once unstable. A second unstable (real) eigenvalue is acquired above the saddle-node. These two unstable eigenvalues then collide almost immediately on the real axis (second filled diamond) and with increasing  $\mu$  move into the complex plane. Thus no stable solutions are present in this regime. However, in the presence of a small drift speed  $c$  the states originating in the pitchfork bifurcation are no longer related by symmetry, and the pitchfork bifurcation becomes an *imperfect* bifurcation [9]. Figure 28 shows the result: there are now three distinct branches of periodic structured states at larger values of  $\mu$ , one of which connects to the primary bifurcation (dashed line) while the other two become *disconnected* (solid line). Of these the primary branch retains the two locations where complex eigenvalues become real,

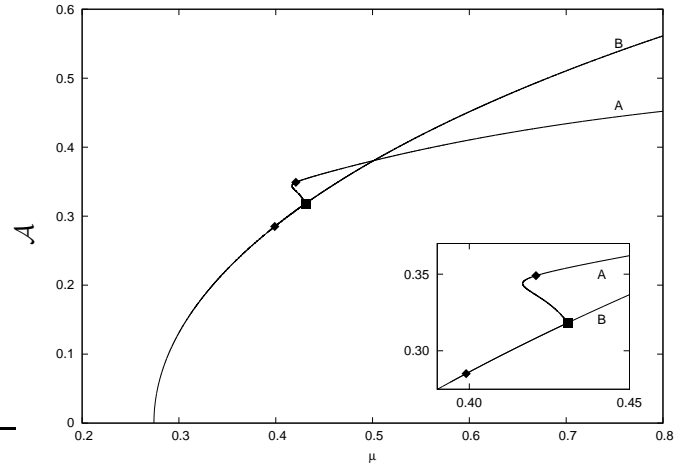


Fig. 27. The single-frequency spatially structured  $n = 1$  branch in the absence of imposed drift. The filled square indicates a pitchfork bifurcation while the filled diamonds mark transitions from a complex conjugate pair of unstable eigenvalues to two unstable real eigenvalues. The inset shows an enlargement of the region where the important transitions take place. All branches shown are unstable. Parameters:  $\lambda = 0.45$ ,  $a = 2.0$ ,  $c = 0$ ,  $L = 6.0$ .

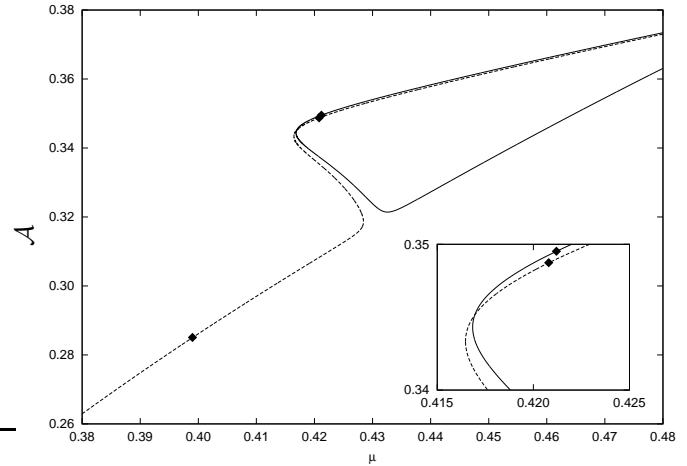


Fig. 28. An imperfect pitchfork bifurcation when  $c = 0.001$  in a domain of size  $L = 6.0$  with  $\lambda = 0.45$ ,  $a = 2.0$ . The disconnected branch is shown as solid to distinguish it from the branch that remains connected to the primary bifurcation (dashed).

while the disconnected branch retains only the upper one.

With further increase in the drift speed  $c$  the pitchfork bifurcation splits apart even more. Figure 29 shows that as this happens the primary branch straightens out, retaining an interval between the two filled diamonds where the two leading eigenvalues are real, while the disconnected branch adopts a form reminiscent of Fig. 19. During this process the location of the remaining filled diamond remains on the original part of the disconnected branch and does not cross the saddle-node even though it now falls below the saddle-node (Fig. 29, inset). As a result on the upper arm of the disconnected branch there is a single (real) unstable eigenvalue. A second unstable eigenvalue is created at the saddle-node and these then collide to form a complex conjugate pair on the lower arm as  $\mu$  increases.

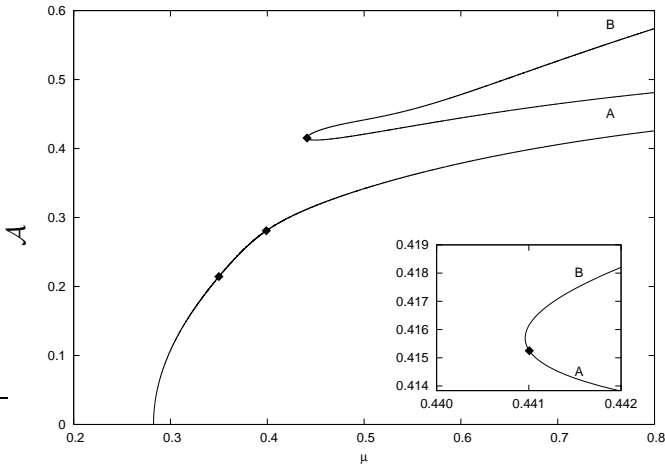
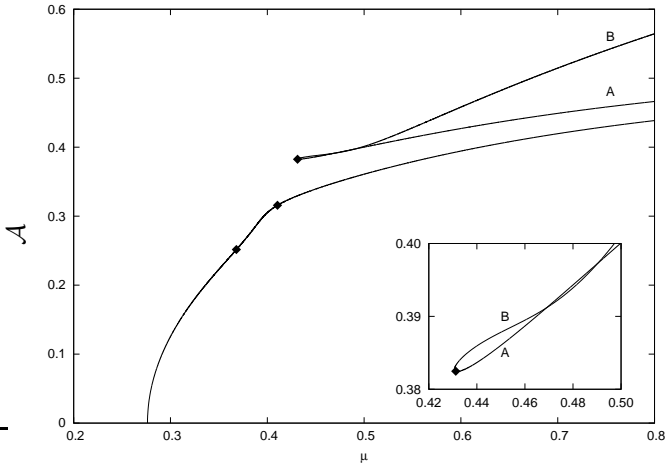


Fig. 29. As for Fig. 28 but for  $c = 0.1$  (top) and  $c = 0.2$  (bottom).

Figure 30 shows the movement of the leading eigenvalues along the branch labeled ‘A’ in Figs. 27-29 and the lower branch of Fig. 31. For  $c = 0$  the leading eigenvalues at large  $\mu$  form a complex conjugate pair that collides with decreasing  $\mu$  on the positive real axis at  $\sigma \approx 0.195$ ; one of the resulting real eigenvalues subsequently increases while the other decreases and passes through zero at the saddle-node. When  $c = 0.2$  the collision occurs at  $\sigma \approx 0.045$ , while for  $c = 0.5$  the eigenvalues first pass through the imaginary axis generating a Hopf bifurcation before colliding in  $\sigma < 0$ . This time it is the larger real eigenvalue that passes through zero at the saddle-node as  $\mu$  decreases. It follows that with increasing  $c$  a Hopf bifurcation appears on the lower arm of the disconnected branch at which the lower arm acquires stability. This stability region stretches from the Hopf bifurcation to the saddle-node bifurcation (Fig. 31) and appears for the first time when  $c$  reaches approximately 0.3. Evidently this point corresponds to the appearance of a Takens-Bogdanov bifurcation on the disconnected branch [10]. The numerical results together with the branch-following computations in §3.3 suggest that the Hopf bifurcation is supercritical, and hence that the resulting two-frequency states are stable, thereby extending the region of stable structured states towards larger  $\mu$ .

These results shed light on the conclusions derived from

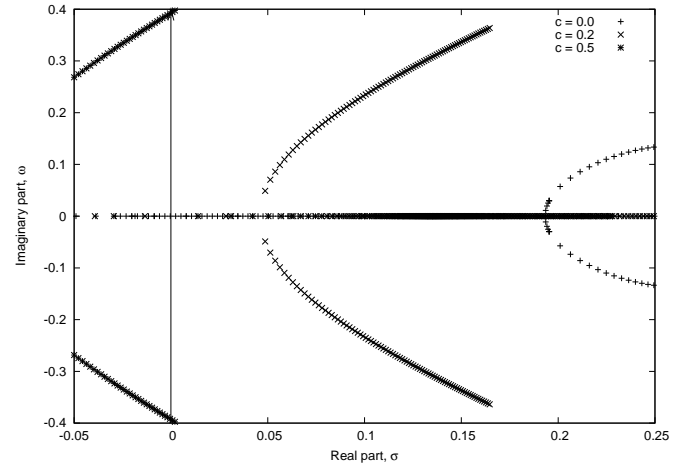


Fig. 30. Eigenvalues  $\sigma \pm i\omega$  in the complex plane along the lower arm of the disconnected branch for  $c = 0, 0.2$  and  $0.5$ . In all cases the imaginary part decreases with decreasing  $\mu$  along the branch.

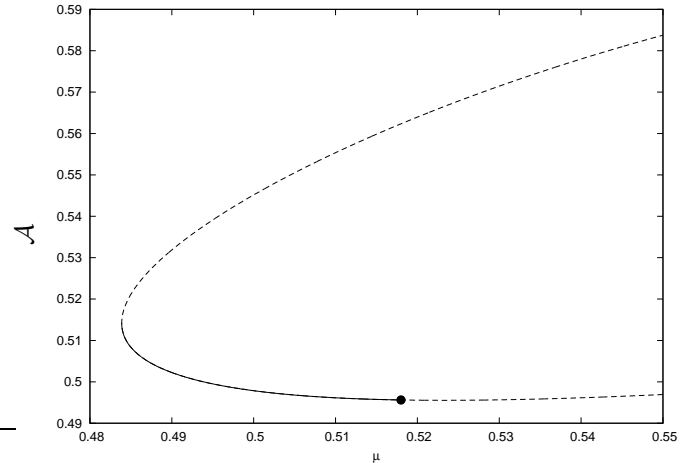


Fig. 31. The disconnected branch when  $c = 0.5$  showing both stable (solid line) and unstable (dashed line) single-frequency states. The filled circle indicates the Hopf (torus) bifurcation.

the direct numerical simulations in the Benjamin-Feir stable regime performed in §2. In that section we noted that for fixed  $c$  and  $\mu < \mu_1$  the structured state always eventually decayed into the stable flat state. In addition, we noted that once  $\mu > \mu_1$  persistent structured states appeared, and that these remained stable for fixed  $c$  not too small provided  $\mu_1 < \mu < \mu_2$ . Based on the results of the present section, admittedly obtained for a smaller domain, we are now in a position to conjecture that the structured states computed in §2 lie on a disconnected branch created by an imperfect bifurcation, and that the lower limit  $\mu_1$  for the presence of *stable* structured states corresponds to the saddle-node bifurcation on this branch provided a Hopf bifurcation is present on the lower arm. Moreover, we attribute the absence of persistent structured states for small  $c$  to the absence of this Hopf bifurcation since it is this bifurcation that is responsible for opening up an interval of stable structured states in the first place. Thus the lowest value of  $c$  for which persistent structured states are present

for *some*  $\mu$  is determined by the location in the  $(\mu, c)$  plane of the codimension-two Takens-Bogdanov bifurcation on the disconnected branch. This conjecture is consistent with the available numerical results.

We expect that similar behavior may be associated with the  $n \geq 2$  primary branches as well, potentially leading to a large multiplicity of coexisting structured states at larger  $\mu$ .

## 5. Conclusions

In this paper we have investigated a well-known equation, the complex Ginzburg-Landau equation with drift, on a finite domain with Neumann boundary conditions. The important feature of these boundary conditions is that they allow the bifurcation of a flat state (a spatially homogeneous oscillation known as the Stokes solution) from the trivial state. In the Benjamin-Feir stable regime these flat states are stable for all values of the forcing parameter. On unbounded (and sufficiently large periodic) domains this flat state coexists with a spatiotemporally chaotic state, just as occurs here on a finite domain with Neumann boundary conditions. However, a careful study showed that the origins of the chaotic state in these two cases differ, and that the two bistable regimes are not in fact related.

On unbounded domains or on periodic domains with a large spatial period the chaotic state is either a phase-turbulent state or defect chaos, depending on the parameters  $\lambda$  and  $a$  in the CGL equation [2]. In contrast, on a bounded domain with Neumann boundary conditions the stable spatially structured states competing with the flat state are periodic, quasiperiodic or chaotic in time, and are the result of an interaction of the drift with the boundaries. Contrary to original expectation we were able to show that these states are not the result of a subcritical Benjamin-Feir instability from the flat states, and found that these states form instead via an imperfect bifurcation from structured states that bifurcate from the trivial state  $A = 0$ . This imperfect bifurcation is a consequence of the drift term, and its net effect is to disconnect a branch of structured states from the primary bifurcation. We showed, in addition, that these states are inevitably all unstable when the drift speed  $c$  is small, but that with increasing  $c$  an interval of stable structured states appears in  $\mu$  even in the Benjamin-Feir stable regime. We showed that the appearance of the stable states is a consequence of a codimension-two bifurcation, the Takens-Bogdanov bifurcation, on the disconnected branch of structured states. This bifurcation opens up a stable interval of single-frequency structured states between the saddle-node and a Hopf bifurcation, and since the latter is supercritical, it opens up an interval of stable two-frequency states as well. It is these states, we believe, that evolve into the complex states identified in larger domains by direct numerical simulation. If this is the case these states are all associated with a branch of structured states that comes in from infinity and returns back to in-

finity, with no connection to either the primary branches bifurcating from  $A = 0$  or the quasiperiodic states bifurcating from the oscillating flat state.

The results of the present work are reminiscent of the properties of circular Poiseuille flow. This flow is linearly stable for all Reynolds numbers, but finite amplitude perturbations trigger complex and persistent response already at modest Reynolds numbers [8,11]. This response appears to be associated with branches of (unstable) single-frequency traveling waves that come in from infinity and return to infinity and the states created in secondary bifurcations from these, much as in the present problem. It is interesting therefore that in hydrodynamics the CGL equation with drift was first derived as an amplitude equation for the instability of plane Poiseuille flow [16] which does possess a finite threshold for linear instability. It is reasonable to speculate that circular and plane Poiseuille flow have fundamentally the same properties except for the absence of a threshold for linear instability in the former case [5]. Indeed, the picture established in Ref. [5] for Poiseuille-Couette flow resembles closely the properties of the flat state of the CGL equation described here, and bifurcations ‘from infinity’ have been studied in the past with precisely this motivation in mind [13]. Equation (1) represents a nontrivial but potentially tractable problem of this kind.

The very complicated behavior displayed by Eq. (1) shows that in the presence of drift terms boundary conditions are of vital importance even in very large domains in determining the types of solution that can be realised. Of course, Neumann boundary conditions represent a singular limit as far as the existence of flat solutions is concerned, and it would be of interest instead to examine Robin-type boundary conditions of the form  $A_x = rA$  for some complex  $r$  in order to identify a distinguished limit in which the different solution branches all fit together.

**Acknowledgment:** This work was supported by EPSRC under grant EP/D032334/1.

## References

- [1] I. S. Aranson, L. Kramer, The world of the complex Ginzburg-Landau equation, *Rev. Mod. Phys.* 74 (2002) 99–143.
- [2] L. Brusch, M. G. Zimmermann, M. van Hecke, M. Bär, A. Torcini, Modulated amplitude waves and the transition from phase to defect chaos, *Phys. Rev. Lett.* 85 (2000) 86–89.
- [3] J. R. Cash, D. R. Moore, A high order method for the numerical solution of two-point boundary value problems, *BIT Numerical Mathematics* 20 (1980) 44–52.
- [4] H. Chaté, Spatiotemporal intermittency regimes of the one-dimensional complex Ginzburg-Landau equation, *Nonlinearity* 7 (1994) 185–204.
- [5] S. J. Cowley, F. T. Smith, On the stability of Poiseuille-Couette flow: a bifurcation from infinity, *J. Fluid Mech.* 156 (1985) 83–100.
- [6] M. C. Cross, P. C. Hohenberg, Pattern formation outside of equilibrium, *Rev. Mod. Phys.* 65 (1993) 851–1112.

- [7] R. J. Deissler, Noise-sustained structure, intermittency, and the Ginzburg-Landau equation, *J. Stat. Phys.* 40 (1985) 371–395.
- [8] B. Eckhardt, T. M. Schneider, B. Hof, J. Westerweel, Turbulence transition in pipe flow, *Ann. Rev. Fluid Mech.* 39 (2007) 447–468.
- [9] M. Golubitsky, D. G. Schaeffer, *Singularities and Groups in Bifurcation Theory, Vol. I*, New York: Springer, 1985.
- [10] J. Guckenheimer, P. Holmes, *Nonlinear Oscillations, Dynamical Systems and Bifurcations of Vector Fields*, New York: Springer, 1984.
- [11] R. R. Kerswell, Recent progress in understanding the transition to turbulence in a pipe, *Nonlinearity* 18 (2005) R17–R44.
- [12] M. R. E. Proctor, S. M. Tobias, E. Knobloch, Noise-sustained structures due to convective instability in finite domains, *Phys. D* 145 (2000) 191–206.
- [13] S. Rosenblat, S. H. Davis, Bifurcation from infinity, *SIAM J. Appl. Math.* 37 (1979) 1–19.
- [14] F. Schilder, H. M. Osinga, W. Vogt, Continuation of quasi-periodic invariant tori, *SIAM J. App. Dyn. Sys.* 4 No. 3 (2005) 459–488.
- [15] F. Schilder, W. Vogt, S. Schreiber, H. M. Osinga, Fourier methods for quasi-periodic oscillations, *Int. J. Numer. Meth. Engng.* 67 (2006) 629–671.
- [16] K. Stewartson, J. T. Stuart, A non-linear instability theory for a wave system in plane Poiseuille flow, *J. Fluid Mech.* 48 (1971) 529–545.
- [17] S. M. Tobias, E. Knobloch, Breakup of spiral waves into chemical turbulence, *Phys. Rev. Lett.* 80 (1998) 4811–4814.
- [18] S. M. Tobias, M. R. E. Proctor, E. Knobloch, The role of absolute instability in the solar dynamo, *Astron. Astrophys.* 318 (1997) L55–L58.
- [19] S. M. Tobias, M. R. E. Proctor, E. Knobloch, Convective and absolute instabilities of fluid flows in finite geometry, *Phys. D* 113 (1998) 43–72.
- [20] M. van Hecke, Building blocks of spatiotemporal intermittency, *Phys. Rev. Lett.* 80 (1998) 1896–1899.